



Inverse characterization of nanoparticle clusters using unpolarized optical scattering without ex-situ measurements



Ozan B. Eriçok, Hakan Ertürk*

Boğaziçi University, Department of Mechanical Engineering, Bebek 34342 Istanbul Turkey

ARTICLE INFO

Article history:

Received 9 February 2017

Revised 23 April 2017

Accepted 25 April 2017

Available online 5 May 2017

Keywords:

Inverse problem

Soot aggregates

Light scattering

Tabu Search

Particle characterization

Nanoparticle

ABSTRACT

Characterization of nanostructures using light scattering experiments without using polarization information and a *priori* particle size or number measurements is investigated through numerical experiments. The study focuses on particle clusters in the form of carbon nanoparticle aggregates that are generated with Filippov's particle-cluster algorithm. Seven cases of monodisperse aggregates with less than 30 nanoparticles with primary particle radius between 10 and 40 nm are investigated, together with one polydisperse case with lognormal particle size distribution. In all these cases, the scattering behavior of an ensemble of well separated, similar aggregates are represented by the behavior of a single aggregate considering orientation averaging using discrete dipole approximation. A database is developed and used for the solution of the direct problem considering the high computational time required for the solution. The inverse characterization problem is formulated as a least squares minimization. Use of Tabu Search algorithm along with gradient based Levenberg–Marquardt algorithm is investigated as problem topology is prone to multiple extrema. It is found that the proposed method relying on Tabu search algorithm is able to predict the particle size and number for monodisperse aggregates with effective radius larger than 20 nm using a UV light source at a wavelength of 266 nm. The proposed method also characterizes the polydisperse aggregate case with reasonable accuracy.

© 2017 Elsevier Ltd. All rights reserved.

1. Introduction

Recent developments on the synthesis of nanoparticles have brought new opportunities to build new nanostructures, which have unique physical properties. These nanostructures are encountered in many diverse areas ranging from biotechnology [1] to combustion [2]. In almost every case, characterization of these nanostructures is a very important task since the parameters such as size, shape and configuration have a great impact on the resulting physical properties or investigated physical phenomena. Black et al. [3] investigated the effects of ^{198}Au nanoparticle shape on their bio-distribution, tumor uptake and intratumoral distribution. They considered four different shapes (nanospheres, nanodisks, nanorods and cubic nanocages) with similar sizes and observed that the nanospheres exhibit the best blood circulation and tumor uptake. However, the nanorods and nanocages reached the core of the tumor better than nanospheres and nanodisks. The processes yielding these structures can be better understood through characterization of these shapes and optimization. Liati et al. [4] made a detailed analysis and characterization of soot particles emitted

by a typical direct injection gasoline engine (GDI) vehicle during New European Driving Cycle (NEDC) and Worldwide harmonized Light duty Test Cycle (WLTC) at various temperature conditions and found that primary soot particles have diameter between 4 and 55 nm.

There are different techniques available to characterize the nanostructures. The most commonly used methods are based on microscopy (TEM, SEM, AFM) [5]. Although these methods are capable of producing high quality images, they may damage the structure [6] and they are not suitable for in-line monitoring. Time-resolved laser-induced-incandescence (TR-LII) is another method to characterize the size distribution of nanoparticles [7]. While it is possible to apply this method for *in-situ* characterization unlike electron microscopy, it is limited only to absorbing nanoparticles and although it is a promising technique there is need for further research to understand some challenging aspects such as the effect of particle composition on LII signals, effect of inhomogeneous particles, or important parameters such as accommodation coefficients related to nano-scale conduction models used for LII [8].

As an alternative, light scattering can be used for characterization of nanostructures. The challenge in light scattering techniques lies in the required rigorous analysis to model scattering of electromagnetic waves through nanostructures. Thus, relying on

* Corresponding author.

E-mail address: hakan.erturk@boun.edu.tr (H. Ertürk).

approximations is a frequently adopted approach. For nanoparticles, Rayleigh–Debye–Gans (RDG) approximation considers light scattering from irregularly shaped particles [9] that is also extended to fractal aggregates (RDG-FA) [10,11]. There are two main approximations of RDG-FA theory: First, $|m - 1| \ll 1$ and $2\pi|m - 1|d_p/\lambda \ll 1$ where m , d_p and λ are the refractive index and primary particle diameter of aggregate, and wavelength of light, respectively, and (2) the effects of multiple scattering and self-induced scattering are neglected. RDG-FA theory is often used in fractal size and morphology characterization [12,13]. Although it is easy to implement, the assumptions of RDG-FA theory are not valid for some aggregates. For example, Köylü and Faeth [14,15] stated that the first assumption may not be held for soot aggregates because of the large refractive index of soot. It was also stated in [16] that although the individual monomers can be considered as Rayleigh scatterers, the soot aggregates cannot be. Moreover, Zhao and Ma [17] showed that the error in angular scattering properties such as S_{11} calculated with RDG-FA method may vary from 1% to 50% near size parameter of 0.4 for a soot aggregate of 128 particles. In another study, Ma [18] also showed that RDG-FA method leads to 10% error while estimating the radius of gyration and fractal dimension of soot.

Another method used to obtain light scattering behavior of the aggregates is T-matrix method [19,20]. Although it is fast, accurate and not limited by the particle size like RDG-FA, only the scattering behavior of non-overlapping aggregates can be calculated by T-matrix method. Therefore, it will not be possible to accurately represent the behavior of aggregates with overlapping particles. Discrete dipole approximation (DDA) introduced by Purcell and Pennypacker [21] is another approach to obtain light scattering behavior of arbitrarily shaped, inhomogeneous scatterers. DDA is a semi-analytical volume integral method and it represents the particles as a finite set of interacting dipoles that gives DDA the flexibility of representing complex geometries with ease. Through the interactions of these dipoles DDA is able to calculate optical behavior of the structure. Further theoretical background about the method can be found in [22]. As a widely adopted method, there are several open source codes available such as DDSCAT [23], ADDA [24], OpenDDA [25], and DDA-SI-v [26].

In some applications light scattering and LII methods are combined. Riemann et al. [27] used LII method to estimate the soot primary particle radius and used that information as an input to ELS method to characterize radius of gyration. Once the primary particle radius and the radius of gyration are obtained the number of nanoparticles in the aggregate can be found from the fractal equation provided that the fractal parameters are known. Then, these values are compared to the TEM measurements and they observed a good agreement on primary particle radius, whereas the values of the radius of gyration and the number of nanoparticles shifted towards larger values. In another study, Huber et al. [28] used Wide-Angle Light Scattering (WALS) and TR-LII methods to find the radius of gyration and primary particle size of the fractal aggregates, respectively. RDG-FA theory is also used in more recent studies. For example, Liu et al. [29] used RDG-FA and generalized Mie-solution method to calculate the absorption and scattering properties of soot aggregates whereas Huber et al. [12] used WALS measurements and Bayesian inference to obtain credible intervals for size and morphology parameters of soot aggregates.

The Mueller matrix determined from the solution of the Maxwell's equations represents the exact scattering behavior of a scatterer by describing the relation between the incident light and scattered light. The matrix itself is a characteristic of a scatterer and a function of the scattering angle and the wavelength of the incident light. Therefore, if the Mueller matrix of a scatterer is known, a rigorous analysis considering its elements can be used for particle characterization via an inverse technique. Mengüç

and Manickavasagam [30] reported that Mueller matrix elements with polarization information such as S_{12} and S_{34} can be used to estimate the number of nanoparticles in the aggregate, N_p , and the primary particle radius, r_p . They outlined a procedure for determining the number of nanoparticles in the aggregate, provided that the primary particle radius is known via an *ex-situ* measurement such as via SEM. Charnigo et al. [31] used the normalized versions of S_{11} , S_{12} , S_{33} and S_{34} and their derivatives up to 5th degree to estimate the agglomeration level. They evaluated the performance of all the elements and their derivatives and found that relying on S_{33} yields the highest among them. In another study, Charnigo et al. [32] used normalized versions of S_{12} and S_{33} and their derivatives to estimate the average nanoparticle diameter. They found that the nanoparticle diameter can be estimated within a 2 nm error if S_{33} is used.

The current state of the art allows light scattering methods to be used in characterization with polarization information and *a priori ex-situ* or *in-situ* measurement via SEM or LII. The objective of this study is to extend the current state of the art by investigating the feasibility of simultaneous estimation of the number of particles and the primary radius, N_p and r_p , of a soot aggregate without using any polarization information or relying on a *priori* measurement. Suspended soot aggregates are considered as an example and numerical experiments are used in this study.

In a light scattering experiment, a volume containing soot aggregates with different morphological parameters are considered. If these aggregates are similar to each other and they form a dilute suspension the scattering behavior of the ensemble can be simulated with the scattering behavior of a single aggregate averaged over multiple orientations as considered in [33–36] and [37]. In this study, all the aggregates in the measurement volume are assumed to be identical and well separated from each other. Moreover, it is also assumed that all the monomers forming the aggregate have the same size. Soot aggregates are often assumed as monodisperse as suggested in [38] and practiced in [12].

The inverse problem considered is formulated as a non-linear least square minimization, where solution is obtained through different optimization techniques. Deterministic methods such as Levenberg–Marquardt and Conjugate Gradient Methods use the gradient information and usually converge relatively faster. However, the problem considered may contain multiple local minima, and predicting the global minimum is not guaranteed by using these methods relying on gradient information. Although stochastic methods or meta-heuristics are usually computationally expensive, they have superior performance in locating a global minimum. Simulated Annealing, Genetic and Tabu Search algorithms are widely used stochastic methods in the literature. This study considers using Levenberg–Marquardt and Tabu Search for the solution of the inverse problem.

2. Theory

2.1. Light scattering

Scattering event is usually formulated with a 4×4 matrix, known as *Mueller matrix* [39], which relates the incident and scattered intensities. All the elements of the *Mueller matrix* are functions of the scattering angle, θ , and the wavelength of the incident light, λ .

Measuring the elements of Mueller matrix may provide the required information to accurately characterize the nanoparticles. Although there are 16 elements in the Mueller matrix, 7 of them that correspond to the four moduli $|S_j|$ ($j = 1, 2, 3, 4$) and three phase difference between S_j are independent. The remaining 9 elements of S_{ij} are related and these relations are derived in [40].

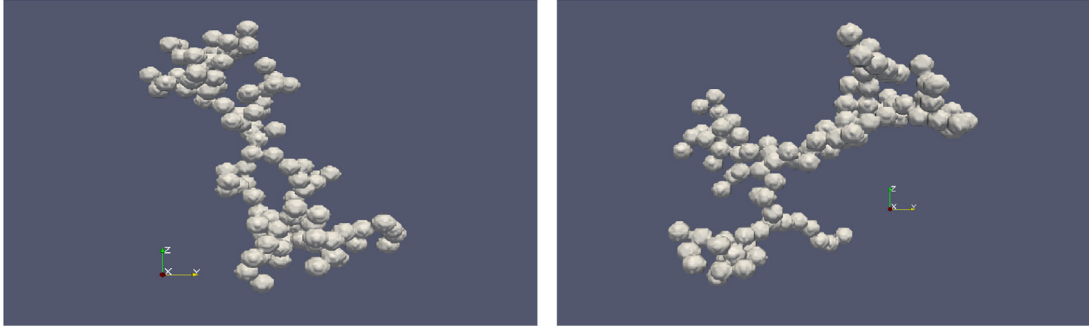


Fig. 1. Two different sample aggregates of 100 particles with $D_f = 1.81$ and $k_f = 1.37$ from the same view angle.

The definition of each individual element of Mueller matrix may help better understand the scattering event. S_{11} represents the differential scattering cross section. If an unpolarized light is incident upon the particle, then S_{11} relates the incident total intensity, I_i , to scattered total intensity, I_s by $S_{11} = I_s/I_i$ with $(kr)^{-2}$ omitted. An equivalent representation is the scattering phase function if it is normalized by the area under $S_{11}-\theta$ curve [39].

2.2. Representation of aggregates

The aggregates can be mathematically represented by the fractal equation,

$$N_p = k_f (R_g/r_p)^{D_f} \quad (1)$$

where N_p is the number of particles in the aggregate, r_p is the primary particle radius, R_g is the radius of gyration, and D_f and k_f are the fractal dimension and fractal prefactor, respectively.

Fractal-like aggregates can be generated by the Filippov's algorithm [41]. There are two main approaches regarding the simulation of the aggregate formation. The particle-cluster algorithm starts with two touching particles and adds one particle at a time to the cluster of nanoparticles. Whereas, in the cluster-cluster algorithm, there are small aggregates generated by particle-cluster algorithm with more or less equal number of primary particles. At each step, these small clusters are connected to each other in a specific way to create one bigger aggregate. While particle cluster algorithm appears to be more suitable for generating smaller aggregates, it is not guaranteed to produce aggregates exactly satisfying the fractal parameters defined using this algorithm as stated by Filippov et al. [41] and Skorupski et al. [42]. Since the main focus of this study is characterization of small aggregates, particle-cluster algorithm is used in this study considering that the fractal parameters for the aggregates are approximately known, which is also typical for aggregate characterization problems. Therefore, despite its uncertainty in satisfying fractal parameters, using particle-cluster algorithm is suitable for this study. Detailed explanations about the particle-cluster algorithm can be found in [42]. An extension of Filippov's particle-cluster algorithm that is used for considering polydispersity on nanoparticle radius is also explained in [42].

The Filippov's particle-cluster algorithm possess randomness that manifests itself in the aggregates generated. Two different aggregates generated with Filippov's particle-cluster algorithm are presented in Fig. 1. Both aggregates contain 100 particles and generated based on morphology parameters $D_f = 1.81$ and $k_f = 1.37$. Their shapes are different due to the randomness of Filippov's algorithm even though all the parameters defining the two aggregates are identical. This observation will be taken into account in calculations.

3. Problem statement

The aggregates considered are assumed to be similar to each other, forming a dilute suspension so that the scattering behavior of the ensemble can be simulated with the scattering behavior of a single aggregate averaged over multiple orientations. This assumption ignores the distribution of number of particles and thus effective radius of aggregates, simplifying the problem. Moreover, in most of the cases considered the particle size distribution for each aggregate is ignored. Therefore, the number of particles, N_p , and the primary particle radius, r_p , of the nanoparticle aggregates will be estimated simultaneously by an inverse technique utilizing the first Mueller matrix element, S_{11} . Strengths and limitations of the proposed method are investigated via numerical experiments. DDA is used to predict the S_{11} in this study considering the limited accuracy of other light scattering models such as RDG-FA. It should be noted that although soot aggregates are considered in this study, the method can be generalized for other materials and geometries as well.

The soot aggregates used in this study are generated by the particle-cluster algorithm described in [42]. The fractal parameters, D_f and k_f , substantially affect the absorption and scattering behavior of soot aggregates as explained in [16] and [43,44]. Different authors suggest different values for D_f and k_f for soot aggregates. The typical value of D_f is reported to be around 1.7–1.8 [45,46]. However, there is no general consensus about the value of k_f . Yon et al. [47] calculated these values from the results of two independent experiments and they reported that $D_f = 1.81$ and $k_f = 1.37$. Therefore, these values are considered as input to the particle-cluster algorithm to generate soot aggregates. However, it should be noted that the aggregates generated by the particle-cluster algorithm would approximate the fractal parameters due to reasons stated in [41] and [42]. Moreover, the fractal equation is not exact for the smaller aggregates that are considered in this study. However, although the generated aggregates are approximate due to both effects discussed, this resembles a more realistic and challenging characterization problem, as real soot aggregates in a volume are not identical and are subject to a variance as mentioned above. Throughout the study, the wavelength of the light is considered as 266 nm as was suggested by Mengüç and Manickavasagam [30], and that is within the UV range of commercial devices. While the optical properties of the soot are adopted from Yon et al. [47], it should be noted that the uncertainty in the refractive index of soot that is discussed by Bond and Bergstrom [48], is not considered in this study.

The typical value for the diameter of an individual monomer constituting the soot aggregate is considered to be less than 50 nm [43]. However, a range of 10–100 nm is suggested for the diameter of a single particle in another study [16]. On the other hand, the range of total number of particles forming the aggregate is quite

Table 1

The cases to test the validity of the proposed inverse method.

Cases	Mean particle radius, r_p (nm)	Number of particles, N_p	Standard deviation, σ_r	Effective radius r_{eff} (nm)
Case 1	33.5	17	0	86.1
Case 2	12.0	8	0	24
Case 3	19.0	12	0	43.5
Case 4	26.0	22	0	72.8
Case 5	40.0	28	0	121.5
Case 6	10.0	4	0	15.8
Case 7	10.0	7	0	19.1
Case 8	15.0	30	1.25	50.3

large, and being less than 1000 particles [18]. However, relatively small number of particles are used in the literature, such as Wu et al. [49] that used soot aggregates with 100 particles in their simulations. Moreover, Tian et al. [38] presented a probability distribution for number of nanoparticles per aggregate based on an experimental study and showed that the probability of aggregates having $N_p < 30$ is higher than others. Several problems are considered in this study to consider the typical range of parameters, as presented in Table 1. The effective radii of an aggregate can be approximated as,

$$r_{eff} = \left(\sum_{i=1}^{N_p} r_i^3 \right)^{1/3} \quad (2)$$

and this relation is simplified to $r_{eff} = r_p N_p^{1/3}$ for uniformly sized aggregates.

The cases considered in this study have effective radius ranging between 15.8 nm and 121.5 nm, and they are selected to identify the strengths and the limitations of the method without losing the physicality of the problem. Cases with smaller particle size and number are considered to test the lower limit of characterization since the values of S_{11} tend to approach the measurement uncertainty as size of the aggregates get smaller. While Cases 1–7 consider monodisperse aggregates comprised of uniform sized particles, the last case, Case 8, considers a polydisperse aggregate comprised of particles having a log-normal size distribution. Therefore, the solution for this case necessitates the prediction of standard deviation along with mean particle size and particle number. The number of particles, mean particle size, and the standard deviation for this case is selected based on data presented [7].

4. Solution methodology

Solution of Maxwell's equations for identifying the Mueller matrix elements for a known geometry and morphology comprises the direct problem in this study. A well-established implementation of DDA, DDSCAT that is developed by Drain and Flatau [23], is used for solution of the direct problem.

4.1. Synthetic measurements

The objective of the current study is to examine the validity of the proposed method via numerical experiments. Therefore, measurements are replaced with synthetic measurements that are comprised of random measurement error introduced simulated measurements. Here, simulated measurements are developed through solution of a direct problem for a set of variables that are to be estimated by the solution of inverse problem. Solution of the direct problem is dependent upon the geometrical orientation of the aggregate with respect to the direction of incident radiation. Therefore, while producing the simulated measurements, the solution of the direct problem is averaged for 490 different orientations of the aggregate relative to the incident light as recommended in [30], in order to avoid such dependency.

It was presented earlier in Fig. 1 that there are geometrical differences between two aggregates defined with exactly the same parameters due to the randomness of the Filippov's particle-cluster algorithm. For each monodisperse case defined in Table 1, ten different fractal geometries are created to identify the effects of the geometrical differences among aggregates. Therefore, a total of 70 different fractal geometries (10 for each of Cases 1–7) are obtained. On the other hand, since the last case considers a polydisperse aggregate 100 different fractal geometries are created for Case 8.

The effect of measurement noise is also considered. The scattering profiles of the 10 different fractal geometries considered for a given monodisperse case would be slightly different from each other. Considering each of these profiles as a simulated measurement, 10 different random error vectors are introduced to each of these simulated measurements to investigate the effect of measurement error. The synthetic measurements for a given case are defined based on the following equation:

$$(\mathbf{S}_{11}^*)_{i,j} = \mathbf{S}_{11,i}(\mathbf{P}) + \mathbf{E}_{i,j} \quad (3)$$

where $\mathbf{P} = [N_p, r_p]$ for monodisperse cases and $\mathbf{P} = [N_p, r_p, \sigma_r]$ for polydisperse case. \mathbf{E} is the error vector that is randomly defined based on Gaussian distribution with zero mean and standard deviation of $\sigma = 0.0001$, considering the uncertainty of a commercial device [50]. Index $i = 1 \dots 10$ represents the fractal geometry and $\mathbf{S}_{11,i}(\mathbf{P})$ is the simulated measurements for fractal geometry i . Hence, introducing 10 different sets of random measurement errors by taking $j = 1 \dots 10$ results in 100 different synthetic measurements for a given case. However, the synthetic measurement for the polydisperse case is obtained by averaging the error added scattering behavior of the individual simulated measurements for each $\mathbf{P} = [N_p, r_p, \sigma_r]$. Although our preliminary analysis showed that 40 aggregate realizations are enough to represent the scattering behavior of the ensemble of the polydisperse aggregates, the synthetic measurement for Case 8 is obtained by averaging $i = 100$ different error added simulated measurements.

There might be several constraints regarding the real-time experiments. For example, measurements near 0° and 180° are highly disturbed by the incident light. Therefore, it is not possible to carry out measurements at $\theta = 0^\circ$ and $\theta = 180^\circ$ in real-time experiments. Gogoi et al. [51] have executed measurements for 10° – 170° with 1° increment whereas Hovenier et al. [52] have measured between 3° and 174° . In this study, the measurement range is taken as 5° – 165° considering the real-time difficulties. The synthetic measurements are created within this range with 8° increment, for a total of 21 measurements. Our preliminary analysis showed that any increment angle with $\Delta\theta < 16^\circ$ yields acceptable results, therefore $\Delta\theta = 8^\circ$ is used as the increment angle in this study.

4.2. Objective function

The proposed method relies on measurements of S_{11} for a given aggregate at N_m polar angles; θ_i , $i = 1 \dots N_m$. The inverse problem can then be defined as predicting the aggregate that would yield these measurements, $\mathbf{S}_{11} = [S_{11}(\theta_1) \dots S_{11}(\theta_m)]^T$. As the fractal dimension

and prefactor are approximately known for soot aggregates, the system can be defined in terms of $\mathbf{P}=[N_p, r_p]$ for monodisperse cases and $\mathbf{P}=[N_p, r_p, \sigma_r]$ for the polydisperse case. Then, the inverse problem can be defined as estimation of these parameters that minimizes the objective function,

$$F(N_p, r_p) = |\mathbf{S}_{11}^* - \mathbf{S}_{11}(\mathbf{P})|^2 \quad (4)$$

where \mathbf{S}_{11}^* represents measurements and $\mathbf{S}_{11}(\mathbf{P})$ is the estimation of \mathbf{S}_{11} for a given set of variables. The inverse problem formulation presented by Eq. (4) is a non-linear least squares minimization problem that can be solved by optimization through gradient based or stochastic methods.

4.3. Database

The computational time required for a direct solution using DDSCAT for a single set of N_p and r_p , averaging 490 orientations is computationally demanding. Solution of such a problem for an aggregate of 15 nanoparticles with a radius of 8 nm, using a total of 4734 dipoles requires 787 s in an 8 core system with 2.50 GHz frequency, using a parallel implementation of DDSCAT. The required computation time increases as the number and size of particles in the aggregate increase due to increasing number of dipoles simulated. Moreover, it is well known that stochastic methods usually necessitate high number of iterations, whereas the gradient based methods require the estimation of Jacobian that might also be computationally demanding. Therefore, solution of an inverse problem necessitating high number of iterations might not be computationally feasible due to significant computation time required for every iteration.

A common practice for solution of similar problems is to establish a database for different configurations and using the information available in the database for optimization [30,53]. Therefore, a database was created considering fifteen different numbers of particles ranging from 3 to 45 with an increment of 3. Similarly, fifteen different particle radii ranging from 3 nm to 45 nm with an increment of 3 nm were considered, assuming that every nanoparticle in the aggregate has the same radii. For each particle size and number combination, twelve different fractal-like nanoparticle aggregates were generated using the particle-cluster algorithm. The resulting geometries are slightly different from each other due to the randomness of the algorithm. For a given N_p and r_p combination, orientation averaged S_{11} are estimated by DDSCAT considering 490 orientations as explained earlier, for all twelve geometries. Therefore, every S_{11} value for a particular scattering angle in the database is the average of 5880 simulations (490 orientations each for 12 different fractal geometries). Moreover, the scattering angles considered while constructing the database range from 0° to 180° with 1° increment, allowing us to use any subinterval with any increment. The database developed for this study is comprised of a total of 225 (15 different numbers of particles and 15 different particle sizes) set of parameters, and cubic splines were used for prediction of intermediate variables. It should be noted that the database can be extended easily for developing a tool capable of providing a solution in a larger domain.

4.4. Optimization methods

The inverse problem is formulated as a non-linear least squares minimization problem and its solution requires using optimization methods. In this work, Levenberg–Marquardt and Tabu Search algorithms are used as examples of gradient-based and stochastic methods, respectively.

4.4.1. The Levenberg–Marquardt (LM) algorithm

LM algorithm is a widely used iterative method, which is capable of solving ill-conditioned nonlinear least squares problems of

parameter estimation using gradient information. Theoretical information and some applications of the method can be found in [54,55]. For the current problem, LM algorithm solves the following equation,

$$\mathbf{P}^{k+1} = \mathbf{P}^k + \left[(\mathbf{J}^k)^T (\mathbf{J}^k) + \mu^k \mathbf{\Omega}^k \right]^{-1} (\mathbf{J}^k)^T [\mathbf{S}_{11}^* - \mathbf{S}_{11}(\mathbf{P}^k)] \quad (5)$$

where $\mathbf{P}^k=[N_p, r_p]^T$ or $[N_p, r_p, \sigma_r]^T$ denotes the unknown vector for the k -th iteration, \mathbf{J} is Jacobian matrix, μ is the damping parameter, $\mathbf{\Omega}$ is a diagonal matrix comprised of diagonal elements of $(\mathbf{J}^k)^T (\mathbf{J}^k)$. The computational algorithm to solve Eq. (5) can be found in [55]. In this work, the initial guess for \mathbf{P} is determined randomly within the domain of unknowns and μ^0 is taken as 0.001 as suggested in [55]. The following criteria were used to stop the iterative procedure,

$$F(\mathbf{P}^{k+1}) < \varepsilon_1 \quad \text{or} \quad |\mathbf{P}^{k+1} - \mathbf{P}^k| < \varepsilon_2 \quad (6)$$

where ε_1 and ε_2 are the defined tolerances. In this study, ε_2 is taken as 10^{-3} , whereas ε_1 is calculated based on,

$$\varepsilon_1^2 = \int_{-\infty}^{+\infty} x^2 \frac{1}{\sigma \sqrt{2\pi}} e^{-\frac{x^2}{2\sigma^2}} N_m dx = N_m \sigma^2 \quad (7)$$

where the integral in Eq. (7) includes all the possible values of the error.

4.4.2. Tabu Search algorithm

While gradient based methods such as LM algorithm converges fast to a minimum, the converged solution could be a local minimum rather than the global for problems with multiple extrema. For such problems, using stochastic global search algorithms is essential. Tabu Search (TS), originally proposed by Glover [56], is a meta-heuristic method, developed to solve combinatorial optimization problems such as the traveling salesman. The basic idea in the TS is to take a set of parameters and search the neighborhood of the current point. After searching the neighborhood, the neighboring point which gives the best objective will be taken as the new point to generate new neighbors. At every step, previously visited points are added to a tabu list to avoid coming back to those points again. These two features help TS escape from the local minima.

Although TS algorithm is originally designed to solve combinatorial optimization problems, not all the problems are combinatorial. The simple idea of TS is extended into Continuous Tabu Search (CTS) algorithm by Siarry and Berthiau [57] to solve the problems which has continuous domain. The CTS algorithm is further expanded into Enhanced Continuous Tabu Search (ECTS) method by Chelouah and Siarry [58]. In this study, the ECTS algorithm presented in [58] is used.

It should be noted that the user defined parameters have significant effect on the solution efficiency in all of the algorithms. In this study, the search domain for monodisperse cases is limited to a square area defined by $N_p=[3, 45]$ and $r_p=[3, 45]$ nm. However, the search domain can be easily extended to a larger area. The solution domain is first normalized so that the normalized domain is defined as $\bar{N}_p=[0, 1]$ and $\bar{r}_p=[0, 1]$. The size of the tabu list and the promising list, l_{tabu} and $l_{\text{promising}}$, are set to 400 and 10, respectively. The radius, r_n , which defines the size of the sub-domain is set to 0.3 for the diversification phase as it is observed that using larger r_n results in better diversification. In the intensification phase, this value is halved at every step to have finer search. In all phases, the sub-domain is divided into $N_n=20$ uniformly spaced concentric spheres and $N_n=20$ neighbors are selected randomly within the domain. The last parameters defining the radius of the tabu and the promising regions are r_t and r_p . If a point is labeled as tabu, the region centered by the point with $r_t=0.01$ is also added to the tabu list. Similarly, if a point is labeled as promising, the region centered by the point with $r_p=0.02$ is added to the

Table 2

The summary of different models and solvers used in this study.

Methods	Model	Solver
Method 1	DP	LM
Method 2	DP	TS
Method 3	DB	LM
Method 4	DB	TS

Table 3

The results of the Case 1 for all methods.

Case 1	Number of objective function evaluations	Time [sec]
Method 1	36 ± 12	16,363 ± 5085
Method 2	1218 ± 274	723,782 ± 143,340
Method 3	105 ± 62	1 ± 0.7
Method 4	11,937 ± 2989	151 ± 38

promising list. Finally, the diversification phase terminates when the maximum number of iterations, $N_{max} = 100$, is reached or the solution satisfies the criterion presented in Eq. (7) for the Method 2. $N_{max} = 500$ is used for Method 4, as this method utilizes the database and computational time is no longer a problem.

In order to understand the feasibility of all possible solution approaches, 4 different methods have been devised based on combination of different alternatives as summarized in Table 2. The considered combinations include solution of direct problem (DP) vs using database (DB), and using Levenberg–Marquardt (LM) vs Tabu Search algorithm (TS). It should be noted that orientation averaged results are used in all methods.

5. Results and discussion

5.1. Sensitivity analysis of S_{11}

Although DDSCAT is a widely used open source code and it was validated numerous times [59] and [60], a verification study was carried out at the beginning of this study by reproducing the results presented in [61] to accurately select the parameters of DDSCAT since they affect both the quality of the simulation and the computational time. After required parameters are studied carefully a sensitivity analysis of S_{11} is carried out.

First, the effects of nanoparticle radius, r_p , the number of nanoparticles forming the aggregate, N_p , and the wavelength of the incident light, λ , on the S_{11} are investigated. The wavelengths investigated are chosen based on those used in experimental studies, where the most encountered wavelengths are 266 nm, 532 nm, 798 nm, and 1064 nm [62,47]. The nanoparticle radii are considered from 15 nm to 60 nm with 15 nm increment, whereas number of nanoparticles are considered from 25 to 100 with 25 increment. These dependencies are investigated by averaging the results of 10 different aggregates and presenting the common logarithm of S_{11} .

Fig. 2 shows the effect of wavelength on scattering behavior for $N_p = 25$ with different sized particles. It can be observed that the S_{11} values tend to decrease, independent of the nanoparticle radius, as the wavelength increases. The similar observation is valid for $N_p = 50, 75$ and 100. It is observed that reliable characterization below 15 nm for an aggregate of 25 nanoparticles may not be possible since both the S_{11} and measurement uncertainty are in the same order of magnitude, 10^{-4} , at $\lambda = 1064$ nm. This observation is crucial for characterization of aggregates with small nanoparticle radius since the order of magnitude of S_{11} will be comparable with the measurement uncertainty if longer wavelengths are used. Therefore, working with shorter wavelengths would be more informative in such cases and $\lambda = 266$ nm is used in this study.

Fig. 3 presents the effect of number of nanoparticles in the aggregate on S_{11} , for $\lambda = 266$ nm. There is approximately one order of magnitude difference between the S_{11} values of $N_p = 25$ and $N_p = 100$ for each particle size considered. The effect of nanoparticle radius on S_{11} at $\lambda = 266$ nm can be observed in Fig. 4. The Figs. 3 and 4 exhibit similar behavior except that the order of magnitude difference between the S_{11} values of $r_p = 15$ nm and $r_p = 60$ nm are larger in Fig. 4.

The analysis shows that S_{11} can be used for characterization purposes. However, there are important limitations. First of all, the choice of the wavelength is critical as it has a strong effect on the order of magnitude of the measurements, especially for aggregates formed by smaller sized particles. Secondly, the measurement uncertainty of the experimental device should be as small as possible to obtain reliable measurements. The order of magnitude of the S_{11} tends to decrease as r_p decreases for a given wavelength. Therefore, there exists a lower limit for reliable characterization that will be addressed in the upcoming sections.

5.2. Evaluation of methods

The computational times required by the methods considered here differ significantly. Since Methods 1 and 2 presented in Table 2, require high computational time a single random error is introduced to the scattering behavior of each monodisperse aggregate, by considering $j = 1$ in Eq. (3) for these methods. Therefore, only 10 different synthetic measurement data sets (relying on 10 aggregates, and using a single random error set) are created for evaluation of these methods. Whereas, 100 different synthetic measurement data sets (relying on 10 aggregates, and using 10 random error sets) are utilized for evaluation of Methods 3 and 4 that do not require high computational time like others.

The evaluation of methods are carried out in two steps: In the first step the performance of the methods summarized in Table 2 are tested rigorously using the Case 1 presented in Table 1. In the second step, the results of methods is then presented for the remaining 6 cases, Cases 2–7, presented in Table 1.

5.2.1. Case 1

The objective function contour and the objective function variation along $r_{eff} = 86.1$ nm line are presented for Case 1 in Fig. 5. The data presented in Fig. 5 is generated by solving direct problem with orientation averaging. It can be observed that the topology has multiple local minima, and it can be foreseen that the LM algorithm might converge to a local minima based on the initial guess. The objective function along the $r_{eff} = 86.1$ nm line also confirms this observation, clearly displaying the existence of local minima.

All methods presented in Table 2 are applied for Case 1 and the results are presented in Fig. 6. As can be observed from Fig. 6, the results estimated by the methods relying on LM (Methods 1 and 3), have high variance. The resulting standard deviations of Methods 1 and 3 for r_p are 2 nm and 5 nm; whereas those for N_p are 8 and 13, respectively. However, the results found by the methods with TS have relatively smaller variance. The resulting standard deviations of Methods 2 and 4 for r_p are 0.7 nm and 0.5 nm; whereas those for N_p are 1 and 0.7, respectively. In summary, the methods relying on LM yield higher standard deviation as they converge to a different local minima in each trial with different initial guesses. The results of both r_p and N_p showed that the Methods 2 and 4 have higher accuracy with relatively small variance in estimating the unknown parameters.

Table 3 shows the number of objective function evaluations and computational time required to converge a solution for each method for Case 1 considering different sets of synthetic data used.

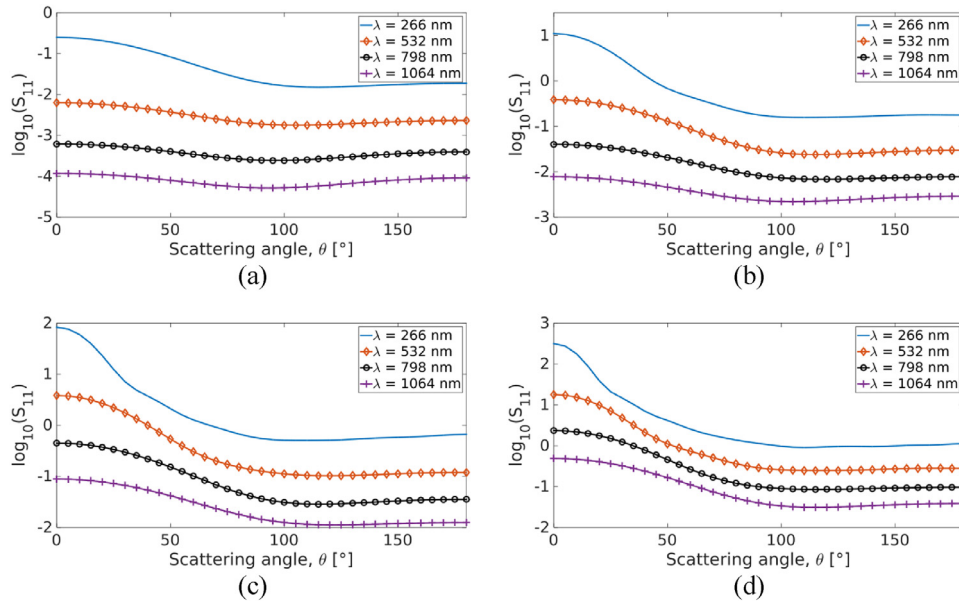


Fig. 2. The effect of wavelength for aggregates of different sized particles, (a) $r_p = 15$ nm, (b) $r_p = 30$ nm, (c) $r_p = 45$ nm and (d) $r_p = 60$ nm, with $N_p = 25$.

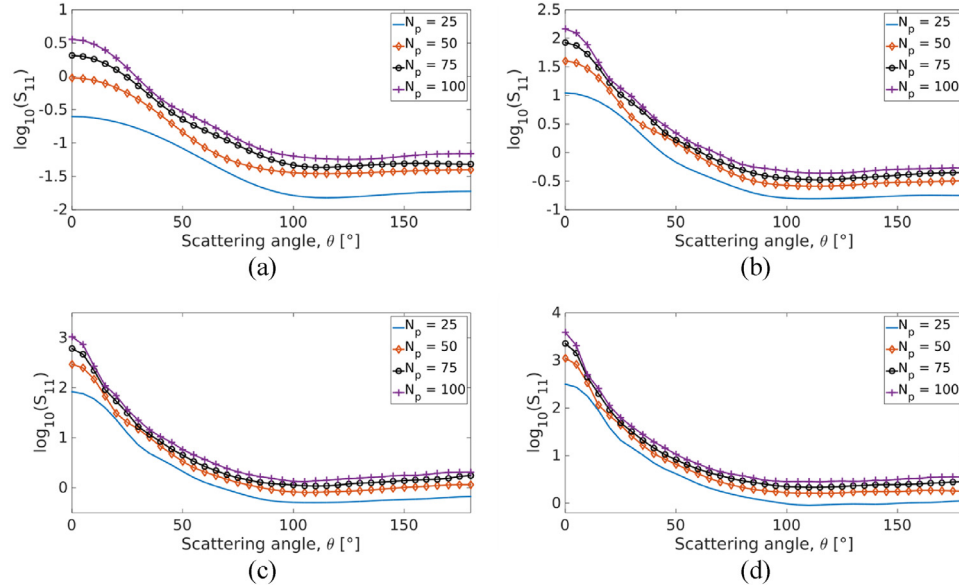


Fig. 3. The effect of number of nanoparticles forming the aggregate for different sized particles, (a) $r_p = 15$ nm, (b) $r_p = 30$ nm, (c) $r_p = 45$ nm and (d) $r_p = 60$ nm, with $\lambda = 266$ nm.

It can be clearly observed that the methods relying on LM algorithm require less objective function evaluations and computational time than methods relying on TS. However, since methods relying on LM, have lower prediction accuracy with higher uncertainty, use of these methods are not recommended for characterization. The computational time and iterations of the other cases are similar to the values presented in Table 3. Therefore, they will not be presented.

It was stated earlier that there exists a randomness in the aggregate generation algorithm, and two aggregates that are generated based on same set of parameters have different aggregate geometries. Moreover, the scattering pattern of aggregates that are generated with different but similar set of parameters might be indistinguishable, identifying a uniqueness problem that limits the precision of the method. Three different parameters sets having the same r_{eff} value, $\mathbf{P} = [13 \ 36.6 \text{ nm}]$, $\mathbf{P} = [17 \ 33.5 \text{ nm}]$ and $\mathbf{P} = [23 \ 30.3 \text{ nm}]$, are considered to further investigate the unique-

ness problem. The 10 different fractal geometries that are created for each parameters sets have different geometries due to the randomness of algorithm used to create aggregates as explained earlier. The forward problem is solved for each 10 fractals sets and the scattering behaviors are estimated. Then, the average scattering profiles and standard deviations of S_{11} values at every scattering angle θ are calculated. The shaded areas in Fig. 7 show the mean \pm standard deviation calculated for each parameter set. Fig. 7 suggests that the range of S_{11} values covered by each parameters sets overlap with each other, especially for the larger polar angles, highlighting the uniqueness problem that limits the precision of the methods proposed.

5.2.2. Cases 2–7

The methods considered are then tested for Cases 2–7 and a summary of the results for all monodisperse cases, based on all the methods are presented in Tables 4 and 5, respectively. Moreover,

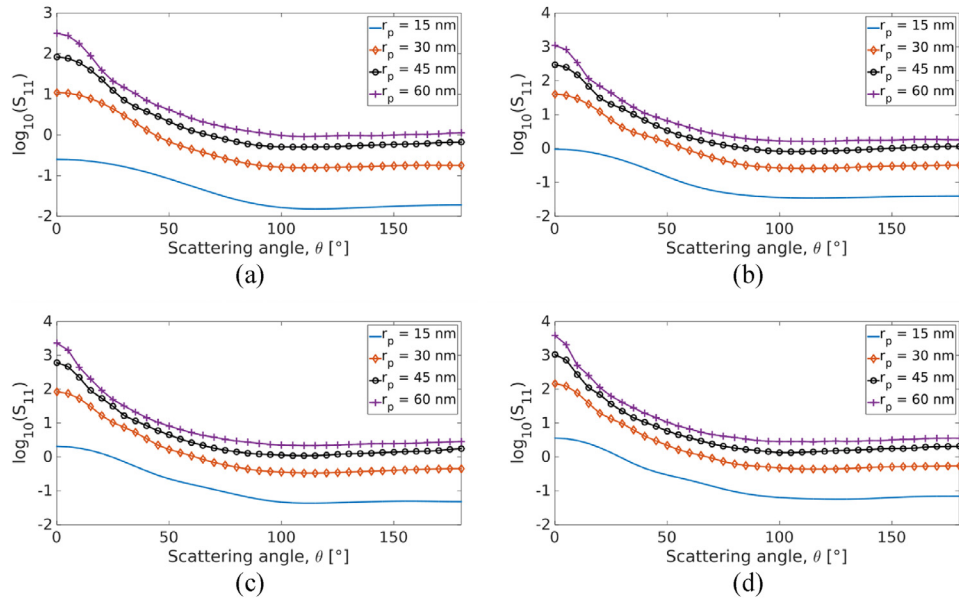


Fig. 4. The effect of nanoparticle radius forming the aggregate, (a) $N_p = 25$, (b) $N_p = 50$, (c) $N_p = 75$ and (d) $N_p = 100$ with $\lambda = 266$ nm.

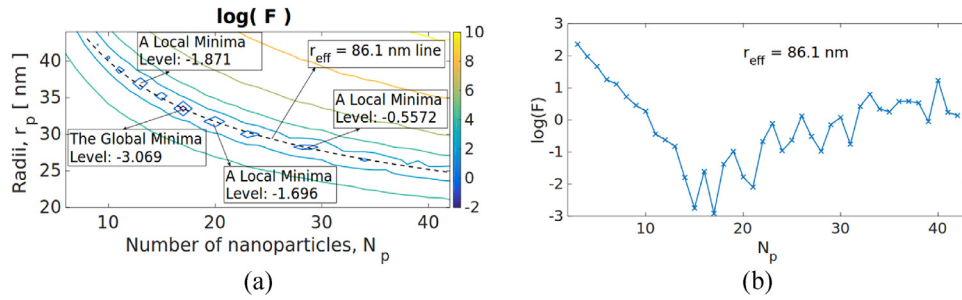


Fig. 5. (a) Natural logarithm of the objective function of Case 1 and (b) objective function along $r_{eff} = 86.1$ nm curve.

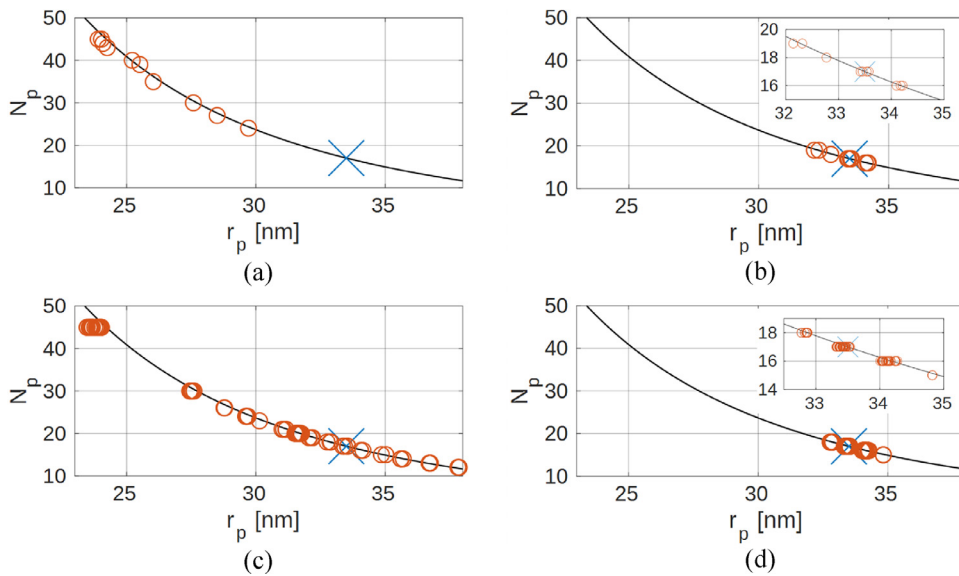


Fig. 6. The results of Case 1 ($N_p = 17$, $r_p = 33.5$ nm) for (a) Method 1, (b) Method 2, (c) Method 3 and (d) Method 4. The blue cross represents the values of Case 1, and the red circles are the predictions based on the corresponding synthetic measurement. The solid line represents the $r_{eff} = 86.1$ nm curve.

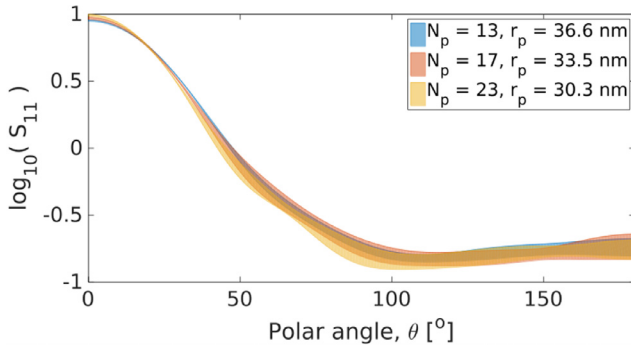


Fig. 7. Uniqueness problem for Case 1.

Table 4

Mean and standard deviation in estimated nanoparticle radius, r_p , for monodisperse cases.

	Estimated radii \pm standard deviation (nm)			
	Method 1	Method 2	Method 3	Method 4
Case 1	25.9 \pm 2.1	33.4 \pm 0.7	28.7 \pm 4.5	33.6 \pm 0.5
Case 2	9.8 \pm 2.0	12.1 \pm 0.7	10.8 \pm 1.4	11.9 \pm 0.4
Case 3	15.6 \pm 3.1	18.4 \pm 0.8	17.0 \pm 2.9	18.8 \pm 0.6
Case 4	25.5 \pm 4.9	26.0 \pm 0.9	24.2 \pm 3.7	26.1 \pm 0.7
Case 5	34.7 \pm 1.2	40.1 \pm 1.1	36.6 \pm 3.2	39.7 \pm 1.3
Case 6	7.2 \pm 1.7	6.5 \pm 1.8	7.2 \pm 1.4	8.7 \pm 1.3
Case 7	6.5 \pm 1.8	7.9 \pm 1.4	8.2 \pm 1.3	9.8 \pm 0.6

Table 5

Mean and standard deviation in estimated number of nanoparticles, N_p , for monodisperse cases.

	Estimated number of nanoparticles \pm standard deviation			
	Method 1	Method 2	Method 3	Method 4
Case 1	37.2 \pm 7.8	17.2 \pm 1.1	29.9 \pm 12.6	16.8 \pm 0.7
Case 2	19.0 \pm 11.1	7.9 \pm 1.4	12.5 \pm 7.3	8.2 \pm 0.9
Case 3	26.3 \pm 12.4	13.3 \pm 1.7	20.3 \pm 11.9	12.4 \pm 1.3
Case 4	27.3 \pm 11.1	22.2 \pm 2.3	30.1 \pm 11.7	21.7 \pm 1.8
Case 5	42.4 \pm 3.9	27.7 \pm 2.3	37.1 \pm 7.8	28.8 \pm 2.4
Case 6	18.5 \pm 7.5	19.4 \pm 9.5	14.8 \pm 7.3	15.1 \pm 10.5
Case 7	31.2 \pm 12.2	17.8 \pm 9.2	15.9 \pm 7.4	5.1 \pm 4.3

the predictions for Cases 2–5 are also presented in Figs. 8–11. The order of magnitude of S_{11} for Cases 6 and 7 are comparable with the sensitivity of measurement device, and the synthetic measurements for these cases are dominated by measurement error. Therefore, their results show high deviation causing large errors and will not be presented here explicitly.

It can be observed from Tables 4 and 5, and Figs. 8–11 that the methods with LM (Methods 1 and 3) fail to consistently converge to the global minimum that represents the correct solution. They converge to different solutions resulting in high prediction uncertainty for radius and number of particles. For the methods relying on TS, Method 2 converges to an acceptable solution in all the cases considered, but it is significantly more computationally expensive. The Method 4 that relies on the database appears to be the most robust, consistent, efficient method with acceptable prediction accuracy. Therefore, using a database with spline fitting can be coupled with the TS algorithm to estimate N_p and r_p of the nanoparticle aggregates.

5.3. Limitations of the method

The limits of a reliable characterization depend on the order of magnitude of S_{11} in comparison to the measurement uncertainty that relies on wavelength of the incident light and aggregate size. As mentioned earlier, the wavelength of the incident light is se-

lected accordingly as 266 nm. Fig. 12 shows the variation in percentage error for predicted r_p and N_p with effective radius, for Method 4 considering all monodisperse cases, for different measurement sensitivity values, σ . It is observed that the prediction errors of both r_p and N_p tend to decrease as r_{eff} increases; whereas, higher errors are observed for N_p in general. Moreover, errors corresponding to Cases 6 and 7 are higher than the rest as they consider smaller aggregates for which the synthetic measurement data is dominated by the introduced measurement error. Higher accuracy predictions are possible by using higher sensitivity measurement devices. Since the error percentages in N_p is higher than that of r_p it can be concluded from Fig. 12(b) that accurate characterization is obtained when $r_{eff} > 27$ nm, $r_{eff} > 20$ nm and $r_{eff} > 18$ nm for $\sigma = 10^{-3}$, $\sigma = 10^{-4}$ and $\sigma = 10^{-5}$, respectively.

5.4. Polydisperse case

It is well known that soot aggregates have a log-normal particle size distribution. While the first 7 cases consider monodisperse aggregates, the final case that considers a polydisperse aggregate with a log-normal particle size distribution constitutes a more challenging problem.

The synthetic measurement for Case 8 is obtained as follows: First, 100 different aggregates with $N_p = 30$ nanoparticles having a log-normal distribution with $r_p = 15$ nm and $\sigma_r = 1.25$ are created. After the scattering behavior of these aggregates is estimated, random measurement error is introduced to each of them. Then, all of these synthetic measurements are averaged to represent the scattering behavior of the ensemble even though our preliminary analysis showed that 40 aggregates are adequate.

The synthetic measurement generated above is tested with Method 4. Since Case 8 includes an additional unknown, standard TS algorithm is slightly modified into nested TS algorithm. Nested TS algorithm first samples different N_p values from the neighborhood of the point considered (outer TS), and then initializes a standard TS (inner TS) to find the optimum r_p and σ_r values for each N_p . The results of the inner TS algorithm are used in the outer TS algorithm to find best N_p values. The points with the best objective function values are stored, and intensification phase begins as usual. The parameters related to inner TS algorithm are adjusted as $r_t = 0.002$, $r_{pr} = 0.004$, $r_n = 0.5$ and $N_n = 50$ whereas same parameters related to outer TS algorithm are adjusted as $r_t = 0.01$, $r_{pr} = 0.01$, $r_n = 0.5$ and $N_n = 6$. The search domain of σ_r is bounded by $\sigma_r = [1 \ 3]$ and normalized like other parameters.

Fig. 13 shows the results of the Case 8 using nested TS that relies on the database created with monodisperse aggregates. The predicted values are $N_p = 22$, $r_p = 16.4$ nm, $\sigma_r = 1.28$ and $r_{eff} = 50.2$ nm. It can be observed that the predicted probability density is close to actual probability density. While the predicted values for r_{eff} , r_p and σ_r are reasonably accurate, the predicted N_p value is less than the actual value. The reason for this deviation in N_p is due to the fact that the effect of smaller particles are obscured by that of larger particles, which makes it harder to capture the actual distribution. Based on this polydisperse case the proposed method can be considered promising for further development.

6. Conclusions

Optical characterization of nanoparticle aggregates via light scattering experiments is investigated. The existing state of the art in aggregate characterization with light scattering relies on polarized light experiments and *a priori* measurements. A method relying on unpolarized light measurements that does not necessitate any prior measurements is proposed and evaluated numerically.

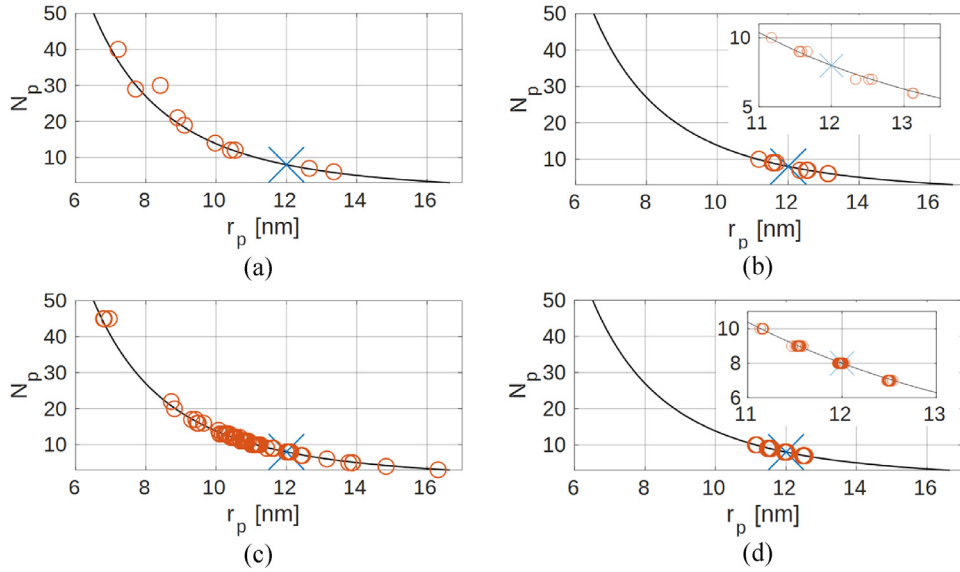


Fig. 8. The results of Case 2 ($N_p = 8$ $r_p = 12$ nm) for (a) Method 1, (b) Method 2, (c) Method 3 and (d) Method 4. The blue cross represents the values of Case 2, and the red circles are the predictions based on the corresponding synthetic measurement. The solid line represents the $r_{eff} = 24$ nm curve.

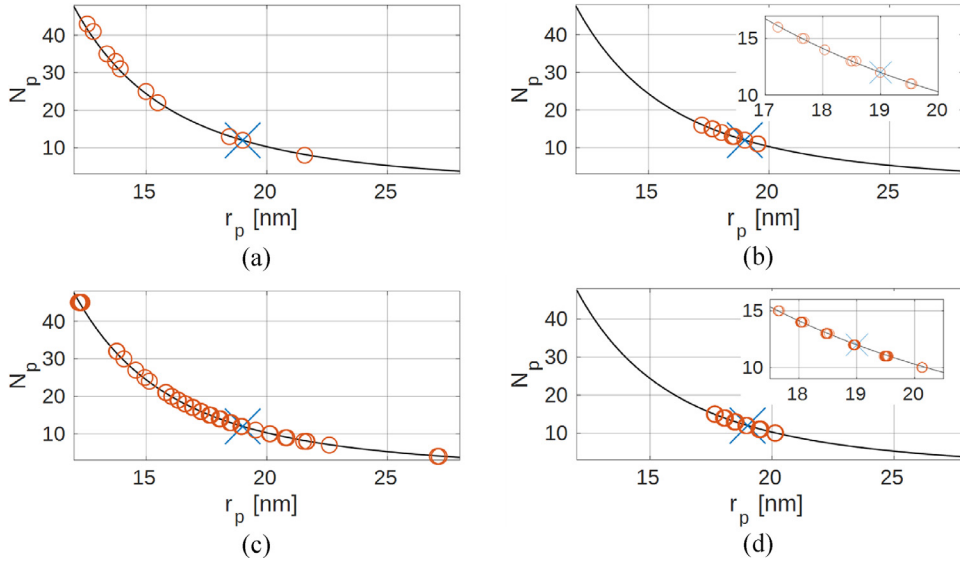


Fig. 9. The results of Case 3 ($N_p = 12$ $r_p = 19$ nm) for (a) Method 1, (b) Method 2, (c) Method 3 and (d) Method 4. The blue cross represents the values of Case 3, and the red circles are the predictions based on the corresponding synthetic measurement. The solid line represents the $r_{eff} = 43.5$ nm curve.

Ensembles of similar and well separated aggregates are considered in this study so that light scattering behavior can be represented by modeling the orientation averaged behavior of a single aggregate using discrete dipole approximation. Filippov's particle cluster algorithm is used to generate the aggregates based on fractal parameters k_f and D_f . While the aggregates generated by the particle-cluster algorithm only approximates the imposed fractal parameters, this resembles a more realistic case. A spline fit to a database is used for predicting the light scattering behavior of different aggregates as estimation of orientation averaged scattering behavior necessitates significant computation time. The inverse problem is formulated as a nonlinear-least squares minimization problem relying on unpolarized scattered intensity that is solved using optimization methods.

A total of eight cases are considered in this study. First seven cases assume monodisperse aggregates with particle radius and

number range of 10–40 nm, and 4–28, respectively. Whereas, the last case considers a polydisperse aggregate with 30 particles with a log-normal size distribution having a mean particle radius of 15 nm, and a standard deviation of 1.25.

It was observed that gradient based techniques such as Levenberg–Marquardt algorithm might converge to erroneous solutions due to the topology with multiple local extrema, and use of global search algorithms is necessary. Therefore, Tabu Search algorithm is applied for the solution of problem. The proposed method is capable of predicting the number of particles and particle radius confidently, down to an effective radius of 20 nm, without using any polarization information or *ex-situ* measurement of particle size or number when a 266 nm light source is used. Moreover, it can also be considered as a promising method for characterizing a polydisperse aggregate as it is able to predict the number of particles, mean particle size and standard deviation of the investi-

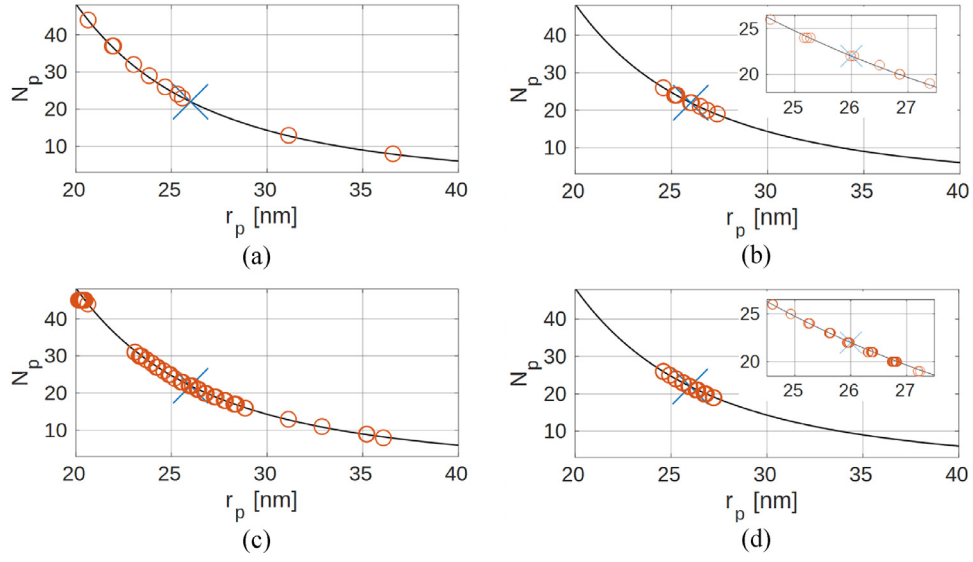


Fig. 10. The results of Case 4 ($N_p = 22$ $r_p = 26$ nm) for (a) Method 1, (b) Method 2, (c) Method 3 and (d) Method 4. The blue cross represents the values of Case 4, and the red circles are the predictions based on the corresponding synthetic measurement. The solid line represents the $r_{eff} = 72.8$ nm curve.

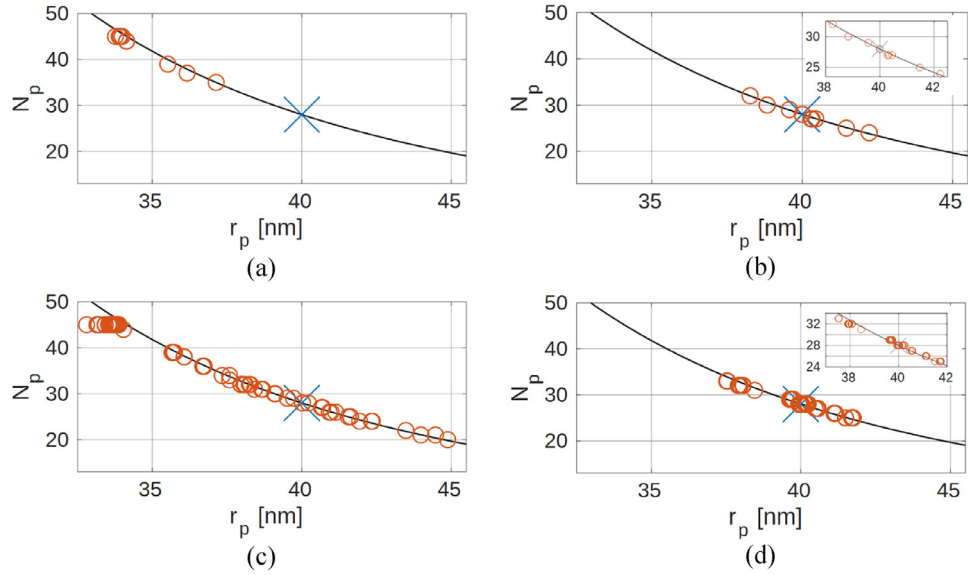


Fig. 11. The results of Case 5 ($N_p = 28$ $r_p = 40$ nm) for (a) Method 1, (b) Method 2, (c) Method 3 and (d) Method 4. The blue cross represents the values of Case 5, and the red circles are the predictions based on the corresponding synthetic measurement. The solid line represents the $r_{eff} = 121.5$ nm curve.

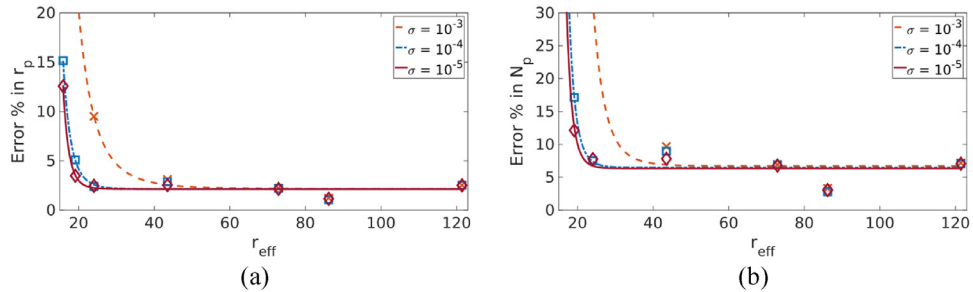


Fig. 12. Average error % values (a) in r_p and (b) in N_p for all cases based on Method 4 for different measurement sensitivity values, σ .

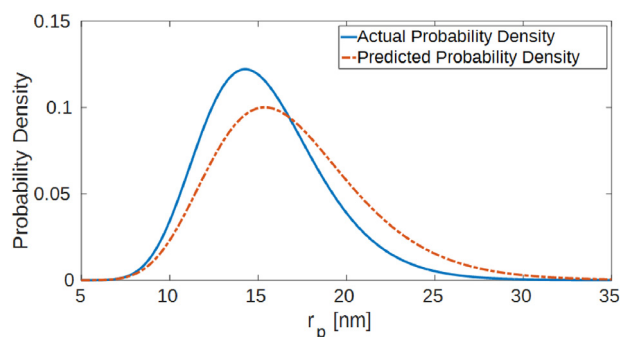


Fig. 13. The results of Case 8 ($N_p = 30$, $r_p = 15$ nm, $\sigma_r = 1.25$) with nested TS algorithm. The blue curve represents the actual probability density of Case 8, and the red dashed-dot curve represents the probability density based on the predicted values, $N_p = 22$, $r_p = 16.4$ nm, $\sigma_r = 1.28$.

gated case with reasonable accuracy. Further research must be carried out to test the method for more polydisperse cases, to further tune the method for improved accuracy, and identify the limits of characterization.

While the results looks promising, there are limitations in the problems considered that needs to be addressed. The characterization limit presented is valid for 266 nm and an increase in characterizable effective radius should be expected when light sources at longer wavelengths such as in visible range are used. Therefore, limiting aggregate size that can be characterized by using different light sources must be identified by a follow up study. Moreover, the current analysis is limited to characterization of well separated, similar aggregates, and it also ignores the uncertainty in the refractive index. Overcoming these limitations requires further research and it might be possible through the use of polarization information that is not used in this study.

References

- [1] Jain PK, Huang X, El-Sayed IH, El-Sayed MA. Noble metals on the nanoscale: optical and photothermal properties and some applications in imaging, sensing, biology, and medicine. *Acc Chem Res* 2008;41(12):1578–86.
- [2] Litton CD, Perera IE. Modeling the optical properties of combustion-generated fractal aggregates. *Fuel* 2014;130:215–20.
- [3] Black KCL, Wang Y, Luehmann HP, Cai X, Xing W, Pang B, et al. Radioactive ^{198}Au -doped nanostructures with different shapes for in vivo analyses of their biodistribution, tumor uptake, and intratumoral distribution. *ACS Nano* 2014;8(5):4385–94.
- [4] Liati A, Schreiber D, Eggenschwiller PD, Dasilva YAR, Spiteri AC. Electron microscopic characterization of soot particulate matter emitted by modern direct injection gasoline engines. *Combust Flame* 2016;166:307–15.
- [5] Mukawa K, Oyama N, Ando H, Sugiyama T, Ogo S, Sekine Y. Synthesis of stable anisotropic carbon particle aggregates covered by surface nano-graphitic sheets. *Carbon* 2015;88:33–41.
- [6] Kozan M, Thangala J, Bogale R, Mengüç MP, Sunkara MK. In-situ characterization of dispersion stability of WO_3 nanoparticles and nanowires. *J Nanopart Res* 2008;10(4):599–612.
- [7] Daun KJ, Stagg BJ, Liu F, Smallwood GJ, Snelling DR. Determining aerosol particle size distributions using time-resolved laser-induced incandescence. *Appl Phys B* 2007;87:363–72.
- [8] Michelsen HA, Schulz C, Smallwood GJ, Will S. Laser-induced incandescence: particulate diagnostics for combustion, atmospheric, and industrial applications. *Prog Energy Combust Sci* 2015;51:2–48.
- [9] Kerker M. The scattering of light and other electromagnetic radiation. New York: Academic Press; 1969.
- [10] Sorensen CM. Light scattering by fractal aggregates: a review. *Aerosol Sci Technol* 2001;35:648–87.
- [11] Faeth GM, Köylü ÜÖ. soot morphology and optical properties in nonpremixed turbulent flame environments. *Combust Sci Technol* 1995;108:207–29.
- [12] Huber FJT, Will S, Daun KJ. Sizing aerosolized fractal nanoparticle aggregates through Bayesian analysis of wide-angle light scattering (WALS) data. *J Quant Spectrosc Radiat Transfer* 2016;184:27–39.
- [13] Sorensen CM, Lu N, Cai J. Fractal cluster size distribution measurement using static light scattering. *J Colloid Interface Sci* 1995;174:45–460.
- [14] Köylü ÜÖ, Faeth GM. Radiative properties of flame-generated soot. *J Heat Transfer* 1993;115:409–17.
- [15] Köylü ÜÖ, Faeth GM. Optical properties of overfire soot in buoyant turbulent diffusion flames at long residence times. *J Heat Transfer* 1994;116:152–9.
- [16] Klusek C, Manickavasagam S, Mengüç MP. Compendium of scattering matrix element profiles for soot agglomerates. *J Quant Spectrosc Radiat Transfer* 2003;79–80:839–59.
- [17] Zhao Y, Ma L. Applicable range of the Rayleigh-Debye-Gans theory for calculating the scattering matrix of soot aggregates. *Appl Opt* 2009;48(3):591–7.
- [18] Ma L. Analysis of error in soot characterization using scattering-based techniques. *Particuology* 2011;9(3):210–14.
- [19] Peterson B, Ström S. T-matrix for electromagnetic scattering from an arbitrary number of scatterers and representations of $E(3)$. *Phys Rev D* 1973;8(10):3661–78.
- [20] Mishchenko MI, Hovenier JW, Travis LD. Light scattering by nonspherical particles: theory, measurements and applications. Academic Press; 1999.
- [21] Purcell EM, Pennypacker CR. Scattering and absorption of light by nonspherical dielectric grains. *Astrophys J* 1973;186(2):705–14.
- [22] Draine BT. The discrete-dipole approximation and its application to interstellar graphite grains. *Astrophys J* 1988;333:848–72.
- [23] Draine BT, Flatau PJ. Discrete-dipole approximation for scattering calculations. *J Opt Soc Amer A* 1994;11(4).
- [24] Yurkin MA, Maltsev VP, Hoekstra AG. The discrete dipole approximation for simulation of light scattering by particles much larger than the wavelength. *J Quant Spectrosc Radiat Transfer* 2007;106(1–3):546–57.
- [25] McDonald J, Golden A, Jennings G. Opendda: a novel high-performance computational framework for the discrete dipole approximation. *Int J High Perform Comput Appl* 2009;23(1):42–61.
- [26] Moghaddam ST, Ertürk H, Mengüç MP. Enhancing local absorption within a gold nano-sphere on a dielectric surface under an AFM probe. *J Quant Spectrosc Radiat Transfer* 2016;178(SI):124–33.
- [27] Riemann J, Kuhlmann SA, Will S. 2D aggregate sizing by combining laser-induced incandescence (LII) and elastic light scattering (ELS). *Appl Phys B* 2009;96(4):583–92.
- [28] Huber FJT, Altenhoff M, Will S. A mobile system for a comprehensive on-line-characterization of nanoparticle aggregates based on wide-angle light scattering and laser-induced incandescence. *Rev Sci Instrum* 2016;87(5).
- [29] Liu F, Wong C, Snelling DR, Smallwood GJ. Investigation of absorption and scattering properties of soot aggregates of different fractal dimension at 532 nm using RDG and GMM. *Aerosol Sci Technol* 2013;47:1393–405.
- [30] Mengüç MP, Manickavasagam S. Characterization of size and structure of agglomerates and inhomogeneous particles via polarized light. *Int J Eng Sci* 1998;36(12–14):1569–93.
- [31] Charnigo R, Francoeur M, Mengüç MP, Brock A, Leichter M, Srinivasan C. Derivatives of scattering profiles: tools for nanoparticle characterization. *J Opt Soc Amer A* 2007;24(9):2578–89.
- [32] Charnigo R, Francoeur M, Kenkel P, Mengüç MP, Hall B, Srinivasan C. Estimating quantitative features of nanoparticles using multiple derivatives of scattering profiles. *J Quant Spectrosc Radiat Transfer* 2011;112(8):1369–82.
- [33] Yurkin MA, Hoekstra AG. The discrete dipole approximation: an overview and recent developments. *J Quant Spectrosc Radiat Transfer* 2007;106:558–89.
- [34] Hull P, Shepherd I, Hunt A. Modeling light scattering from diesel soot particles. *Appl Opt* 2004;43(17):3433–41.
- [35] Karlsson A, Yi T, Bengtsson P. Absorption and scattering of light from ensembles of randomly oriented aggregates. *J Opt Soc Amer A* 2013;30:316–24.
- [36] Berg MJ, Sorensen CM. Internal fields of soot fractal aggregates. *J Opt Soc Amer A* 2013;30(10):1947–55.
- [37] Liu F, Smallwood G. Radiative properties of numerically generated fractal soot aggregates: the importance of configuration averaging. *J Heat Transfer* 2010;132:023308-1-023308-6.
- [38] Tian K, Liu F, Thomson KA, Snelling DR, Smallwood GJ, Wang D. Distribution of the number of primary particles of soot aggregates in a nonpremixed laminar flame. *Combust Flame* 2004;138:195–8.
- [39] Bohren CF, Huffman DR. Absorption and scattering of light by small particles. Weinheim: Wiley-VCH; 2004.
- [40] Abhyankar KD, Fymat AL. Relations between the elements of the phase matrix for scattering. *J Math Phys* 1969;10:1935–8.
- [41] Filippov AV, Zurita M, Rosner DE. Fractal-like Aggregates: relation between morphology and physical properties. *J Colloid Interface Sci* 2000;229(1):261–73.
- [42] Skorupski K, Mroczka J, Wriedt T, Riefler N. A fast and accurate implementation of tunable algorithms used for generation of fractal-like aggregate models. *Physica A* 2014;404:106–17.
- [43] Prasana S, Riviere Ph, Soufiani A. Effect of fractal parameters on absorption properties of soot in the infrared region. *J Quant Spectrosc Radiat Transfer* 2014;148:141–55.
- [44] Liu L, Mishchenko MI, Arnott WP. A study of radiative properties of fractal soot aggregates using the superposition T-matrix method. *J Quant Spectrosc Radiat Transfer* 2008;109:2656–63.
- [45] Sorensen CM, Hageman WB. Two-dimensional soot. *Langmuir* 2001;17(18):5431–4.
- [46] Dobbins RA. Hydrocarbon nanoparticles formed in flames and diesel engines. *Aerosol Sci Technol* 2007;41(5):485–96.
- [47] Yon J, Lemaire R, Therssen E, Desgroux P, Coppalle A, Ren KF. Examination of wavelength dependent soot optical properties of diesel and diesel/rapeseed methyl ester mixture by extinction spectra analysis and LII measurements. *Appl Phys B* 2011;104(2):253–71.
- [48] Bond TC, Bergstrom RW. Light absorption by carbonaceous particles: an investigative review. *Aerosol Sci Technol* 2006;40(1):27–67.

- [49] Wu Y, Cheng T, Zheng L, Chen H. Effect of morphology on the optical properties of soot aggregated with spheroidal monomers. *J Quant Spectrosc Radiat Transfer* 2016;168:158–69.
- [50] Hinds Instruments, Technology for polarization measurement Exicor 150XT, pp. 1–3.
- [51] Gogoi A, Ahmed GA, Das G, Karak N, Boruah R, Choudhury A. Laboratory measurements of the light scattering properties of bentonite clay particles embedded in a cylindrical polymer matrix. *J Mod Opt* 2013;60(8):603–10.
- [52] Hovenier JW, Volten H, van der Zande WJ, Waters LBFM. Laboratory studies of scattering matrices for randomly oriented particles: potentials, problems, and perspectives. *J Quant Spectrosc Radiat Transfer* 2003;79(SI):741–55.
- [53] Baneshi M, Maruyama S, Komiya A. Infrared radiative properties of thin polyethylene coating pigmented with titanium dioxide particles. *J Heat Transfer* 2010;132(2):023306.
- [54] Alifanov OM. Inverse heat transfer problems. Springer Verlag; 1994.
- [55] Özişik MN, Orlande HRB. Inverse heat transfer. Taylor & Francis; 2000.
- [56] Glover F. Tabu Search – Part I. *ORSA J Comput* 1989;21(3):4–32.
- [57] Siarry P, Berthiau G. Fitting of Tabu Search to optimize functions of continuous variables. *Int J Numer Methods Eng* 1997;40(13):2449–57.
- [58] Chelouah R, Siarry P. Tabu search applied to global optimization. *Eur J Oper Res* 2000;123(2):256–70.
- [59] Ayrancı I, Vaillon R, Selçuk N. Performance of discrete dipole approximation for prediction of amplitude and phase of electromagnetic scattering by particles. *J. Quant Spectrosc Radiat Transfer* 2007;103:83–101.
- [60] Yon J, Roze C, Girasole T, Coppalle A, Mees L. Extension of RDG-FA for Scattering Prediction of Aggregates of Soot Taking into Account Interactions of Large Monomers. *Part Part Syst Char* 2008;25:54–67.
- [61] Loke VLY, Huda GM, Donev EU, Schmidt V, Hastings JT, Mengüç MP, et al. Comparison between discrete dipole approximation and other modelling methods for the plasmonic response of gold nanospheres. *Appl Phys B* 2014;115(2):237–46.
- [62] Xu C, Cai X, Zhang J, Liu L. Fast nanoparticle sizing by image dynamic light scattering. *Particuology* 2014;19:82–5.